ACS Photonics

Article

pubs.acs.org/journal/apchd5

Plasmonic Nanohole Arrays on a Robust Hybrid Substrate for Highly Sensitive Label-Free Biosensing

Arif E. Cetin,[†,⊥] Dordaneh Etezadi,[†] Betty C. Galarreta,[‡] Mickael P. Busson,[†] Yasa Eksioglu,[†,§] and Hatice Altug*[,†]

[†]Bioengineering Department, Ecole Polytechnique Federale de Lausanne (EPFL), Lausanne CH-1015, Switzerland

[‡]Departamento de Ciencias-Quimica, Pontificia Universidad Catolica del Peru, Avenida Universitaria 1801, Lima 32, Peru

[§]Institute of Physical Engineering, Faculty of Mechanical Engineering, Brno University of Technology, Technicka 2, 616 69 Brno, Czech Republic

[⊥]Koch Institute for Integrative Cancer Research, Massachusetts Institute of Technology, Cambridge, Massachusetts 02139, United States

Supporting Information

ABSTRACT: Plasmonic nanohole arrays have received significant attention, as they have highly advantageous optical properties for ultrasensitive and label-free biosensing applications. Currently, most of these subwavelength periodic apertures are mainly implemented on transparent materials, which results in multiple spectrally close transmission resonances. However, this spectral characteristic is not ideal for biosensing applications, as it complicates monitoring spectral variations. In this article, utilizing a hybrid substrate composed of a high refractive index dielectric interlayer over a transparent material, we show that gold nanohole arrays support spectrally isolated and well-defined plasmonic resonances that are easy to track. Compared to conventional configurations on transparent material, nanoholes on a hybrid substrate also exhibit plasmonic modes with well-preserved amplitudes, which is useful for reliable spectral monitoring. We show that nanohole arrays on a hybrid substrate are more sensitive to changes in surface conditions. Using a spectral integration method, which evaluates wavelength shifts in a large spectral window instead of monitoring only the plasmonic resonance wavelength, we obtain a detection limit as low as 2×10^{-5} RIU. Furthermore, we successfully demonstrate real-time monitoring of biomolecular binding interactions even at sub-1 ng/mL levels.

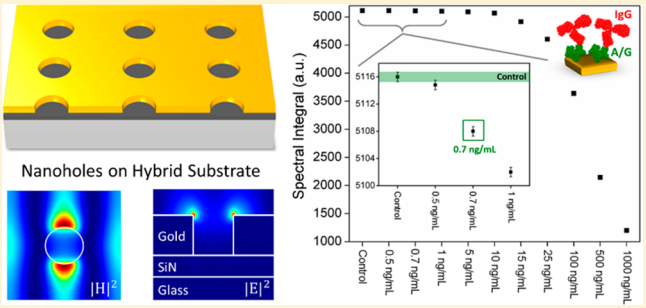

KEYWORDS: *plasmonics, ultrasensitive biodetection, label-free sensing, refractive index sensitivity, spectral integration, nanofabrication*

Biosensors are essential in preventing epidemics for public and global health, warning of intentionally released agents for national security and defense, and fundamental biology and pharmacology research for early disease detection and drug discovery. These applications require biosensors that possess several critical properties for reliable and rapid detection. For instance, label-free biosensors can eliminate problems associated with labeling steps.[1] Biosensors with ultrasensitive optical responses can accurately distinguish minute changes in molecular level.[2−5] The ability to operate in real-time can enable analysis of biomolecular binding kinetics.[6] Massively multiplexed biosensors can allow parallel screening of a large variety of biological assays.[7] Portable biosensors that are easy to operate in a cost-effective manner can be used in resource-poor settings.[8] Recently, plasmonic biosensors utilizing nanoparticle and nanoaperture geometries have received significant attention, as they can meet these needs. In particular, nanohole arrays fabricated on optically thick metal films are highly promising.[9−17] These subwavelength apertures enable extraordinary optical transmission (EOT) phenomenon due to the effective excitation of plasmons at normal incidence by grating coupling. This feature allows compact biosensors by eliminating the bulky prism-coupling mechanism needed by conventional surface plasmon resonance (SPR) sensors.[18,19] Even though SPR schemes have a very sensitive response of around 10^{-7} RIU (refractive index unit), their angle-sensitive optical setup limits large-area multiplexing and high-throughput biodetection. Plasmonic modes supported by nanohole arrays are highly sensitive to surface conditions due to their strong field enhancements and light confinement in nanometer scale.[20] Consequently, local refractive index changes induced by the binding of minute quantities of biomolecules on the sensor surface can be detected by monitoring the spectral variations within the plasmonic modes without any need for fluorescent labels. Nanohole arrays are also compatible with imaging-based

Received: May 5, 2015
Published: July 29, 2015

DOI: 10.1021/acsphotonics.5b00242
ACS Photonics 2015, 2, 1167−1174

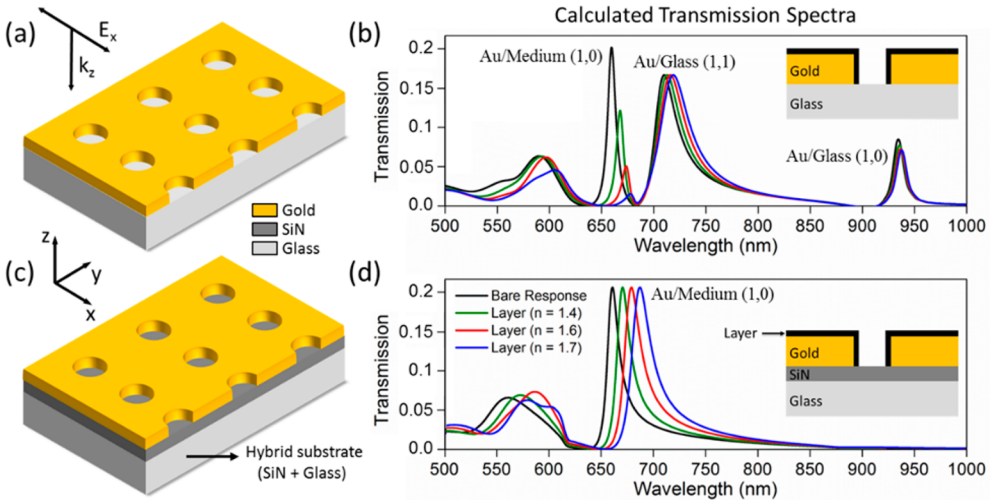

Figure 1. Schematic illustration of the gold nanohole arrays on (a) glass (fused silica with refractive index 1.42) and (c) hybrid substrate (Hybrid substrate = SiN + Glass). Propagation and polarization directions of the illumination source used in the numerical calculations are shown in the figure. Calculated transmission spectra of the nanohole arrays on (b) glass and (d) hybrid substrate, where the gold surface is covered with an 8 nm thick dielectric analyte layer (illustrated with black in figure insets) with refractive indices n = 1.4, n = 1.6, and n = 1.7. The medium above the sensor coated with a thin dielectric layer is air. The aperture system on glass supports Au/Medium(1,0) [Medium = Air], Au/Glass(1,1), and Au/Glass(1,0) modes, while the one on a hybrid substrate supports only the Au/Medium(1,0) mode [Medium = Air]. The plasmonic mode of interest used in the sensing of the thin analyte layer is Au/Medium(1,0) [Medium = Air]. Corresponding device parameters used in the simulations: hole diameter 200 nm, array periodicity 600 nm, thicknesses of the gold film and silicon nitride interlayer 120 and 70 nm, respectively.

devices and can be implemented in a microarray format for multiplexed and high-throughput biosensing.[21] The excitation[22−29] and collection of optical transmission through nanohole array gratings could be achieved in optical set-ups that are cost-effective and portable. Recently, plasmonic nanoholes have been utilized in a lens-free microscope with a normally incident light-emitting-diode (LED) source and a complementary metal-oxide semiconductor (CMOS) camera to demonstrate a low-cost hand-held biosensor for resource-poor and field settings.[8,30] Integrating with microfluidic systems, nanohole biosensors also enable real-time analysis of biomolecular binding kinetics.[11,30]

So far, most nanohole designs are implemented directly on transparent materials, i.e., glass (Figure 1a). Figure 1b shows the EOT response of periodic nanohole arrays on glass covered with a thin layer of dielectric analyte of varying refractive indices. The EOT spectra have multiple resonance peaks that are spectrally close to each other. However, this is not well-suitable for biosensing applications requiring reliable and accurate identification of spectral shifts. For instance, due to the differences in the sensitivity of different plasmonic modes, their spectra start to merge, which makes monitoring spectral variations difficult. Furthermore, the amplitude of the most sensitive mode, Au/Medium(1,0) [Operation Medium = Air], significantly decreases as the refractive index of the analyte layer increases. This problem could be overcome by utilizing nonperiodic nanoholes, as they could support a single transmission resonance. However, the spectral line width of their resonance is larger, which compromises their biosensing performance. Herein, we demonstrate that inserting a high index dielectric material, e.g., a silicon nitride interlayer between the metallic film and the transparent supporting substrate (Figure 1c), overcomes these problems. Using this hybrid substrate consisting of a silicon nitride (SiN) interlayer on glass, we obtain spectrally isolated and well-defined EOT signals that are easy-to-track. Compared to the conventional configuration on glass, in our nanoaperture system the amplitude of the transmission resonances is well-preserved (Figure 1d). We also show that the nanoholes on the hybrid substrate support higher sensitivities. By utilizing a spectral integration method, in which the total shift in a spectral window instead of only the resonance peaks is monitored, we observe dramatic sensitivity improvements. Using this integration method, we experimentally demonstrate a detection limit as low as 2×10^{-5} RIU and real-time analysis of biomolecular binding interactions even below 1 ng/mL analyte concentration levels.

NANOHOLE ARRAYS ON GLASS AND HYBRID SUBSTRATES

Figure 1a and c illustrate the gold nanohole designs utilizing a glass and hybrid substrate, respectively. Figure 1b and d show their transmission spectra calculated for an x-polarized light source (black curves denote the bare response without analyte layer). Numerical analyses are performed with finite difference time domain (FDTD) calculations (Lumerical Solutions, Inc.; see Supporting Information for simulation details). Nanohole arrays can support multiple resonances at peak wavelengths (λ_{res}) obeying the grating coupling condition

$$\lambda_{res} = \frac{P}{\sqrt{i^2 + j^2}} \sqrt{\frac{\varepsilon_d \varepsilon_m}{\varepsilon_d + \varepsilon_m}} \quad (1)$$

where ε_d and ε_m are the permittivity of the dielectric and metal, P is the periodicity of the square array, and (i, j) are the grating orders along the x- and y-directions. For the given spectral range, the nanohole system on glass with a 200 nm hole diameter, 600 nm array periodicity, and 120 nm gold thickness supports three distinct transmission resonances due to Au/Medium(1,0) [Medium = Air], Au/Glass(1,1), and Au/Glass(1,0) mode excitations spectrally peaked at ∼660, ∼710, and ∼934 nm, respectively. On the other hand, the one on a hybrid substrate, utilizing a 70 nm thick silicon nitride interlayer on top of glass, supports only the Au/Medium(1,0) mode

DOI: 10.1021/acsphotonics.5b00242
ACS Photonics 2015, 2, 1167−1174

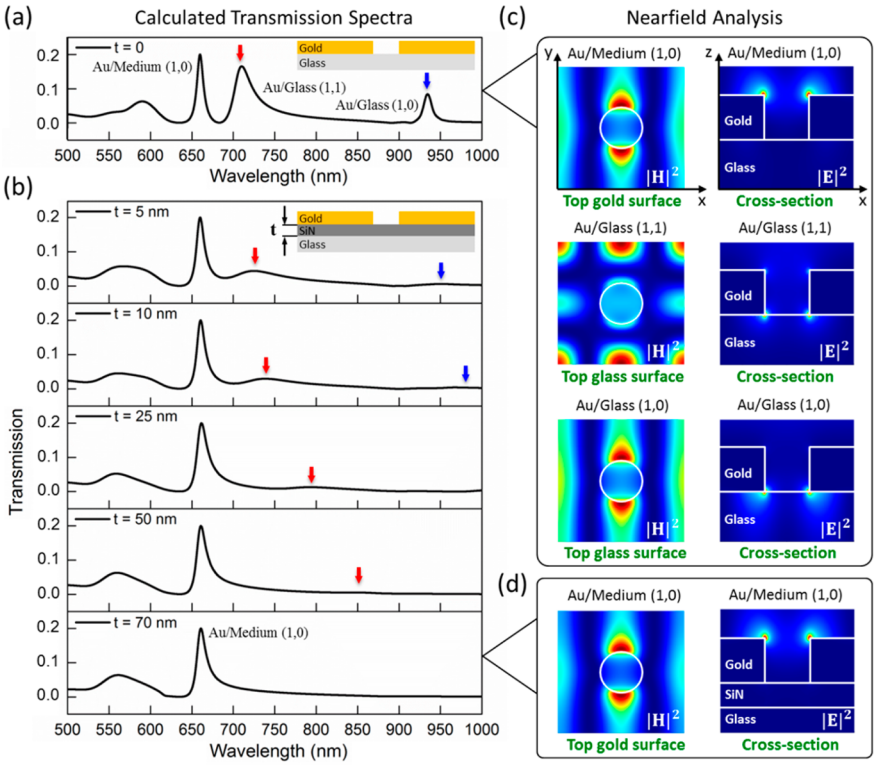

Figure 2. Calculated transmission spectra of the nanohole arrays on (a) glass and (b) hybrid substrate, where the thickness of the silicon nitride interlayer (t) is varied from 5 to 70 nm, as schematically illustrated in the inset [medium above the structure is air, i.e., Medium = Air]. In panel b, red and blue arrows highlight the suppression of Au/Glass modes with increasing silicon nitride thickness. Magnetic ($|H|^2$) and electric ($|E|^2$) field intensity distributions calculated at the corresponding transmission resonances for the aperture system on (c) glass and (d) hybrid substrate with a 70 nm thick silicon nitride interlayer.

[Medium = Air] at ~660 nm, and Au/Glass modes are no longer observed.

In order to compare the sensitivity of the nanoaperture systems, we perform FDTD simulations with an 8 nm thick dielectric layer (denoted with black in Figure 1b–d, inset) covering only the gold film. Figure 1b and d show the transmission spectra of the two nanohole configurations in the presence of 8 nm thick analyte layer with the refractive indices n = 1.4 (green curve) and n = 1.6 (red curve). The medium above the analyte covered gold sensor is air, which is indicated below as Medium = Air. For the aperture system on glass with n = 1.4 [n = 1.6], the Au/Medium(1,0), Au/Glass(1,1), and Au/Glass(1,0) modes shift by ~8 nm [~14 nm], ~2 nm [~6 nm], and ~2 nm [~3 nm], respectively. The Au/Medium(1,0) mode provides the highest sensitivity compared to the others due to its more accessible large local electromagnetic fields, which will be discussed in the next section. As the Au/Medium(1,0) mode [Medium = Air] shifts to longer wavelengths, we observe a dramatic reduction in the transmission intensity due to its increasing spectral overlap with the Au/Glass(1,1) mode. This overlap is due to the difference between the sensitivities of Au/Medium(1,0) [Medium = Air] and Au/Glass(1,1) modes, in which the latter one shifts less. Importantly, when the refractive index of the thin analyte layer on the sensor surface is increased to n = 1.7 (blue curve), the transmission intensity of the Au/Medium(1,0) mode [Medium = Air] strongly diminishes since the Au/Glass(1,1) mode has a much larger transmission intensity compared to the Au/Medium(1,0) mode [Medium = Air]. In contrast, nanoholes on a hybrid substrate support only the Au/Medium(1,0) mode [Medium = Air] within the presented spectral window. The system also shows higher sensitivities; that is, the Au/Medium(1,0) mode [Medium = Air] red-shifts by as much as ~11 and ~19 nm for the refractive indices of the dielectric layer n = 1.4 and n = 1.6, respectively. In the absence of any spectral merging between different transmission resonances, the Au/Medium(1,0) mode [Medium = Air] shifts to longer wavelengths with negligible amplitude variations. These features make the nanohole system on the hybrid substrate highly suitable for biosensing applications.

ELIMINATION OF MULTIPLE PLASMONIC MODES

In order to understand how the multiple transmission resonances corresponding to Au/Glass modes are suppressed by a thin silicon nitride interlayer, we investigate the near-field characteristics of the modes supported by the nanoholes for both substrates. As shown in Figure 2a, for the nanohole system on glass, the Au/Glass(1,1) mode (indicated by a red arrow) is spectrally located very close to the most sensitive Au/Medium(1,0) mode [Medium = Air] since glass (fused silica) has a low refractive index, n_{glass} = 1.42. For the hybrid substrate, this mode is suppressed by the higher effective refractive index of the supporting layer (silicon nitride, n_{SiN} = 2.16) with increasing silicon nitride thickness (t), as shown in Figure 2b. Figure 2c and d show the corresponding magnetic ($|H|^2$) and electric ($|E|^2$) field intensity distributions calculated at the plasmonic resonances for both nanohole configurations. For the apertures on glass (t = 0), we obtain the magnetic field intensity profiles at the air/metal interface (top surface of the metal film) for the Au/Medium mode [Medium = Air] and at the metal/glass interface (bottom surface of the metal film) for

DOI: 10.1021/acsphotonics.5b00242
ACS Photonics 2015, 2, 1167–1174

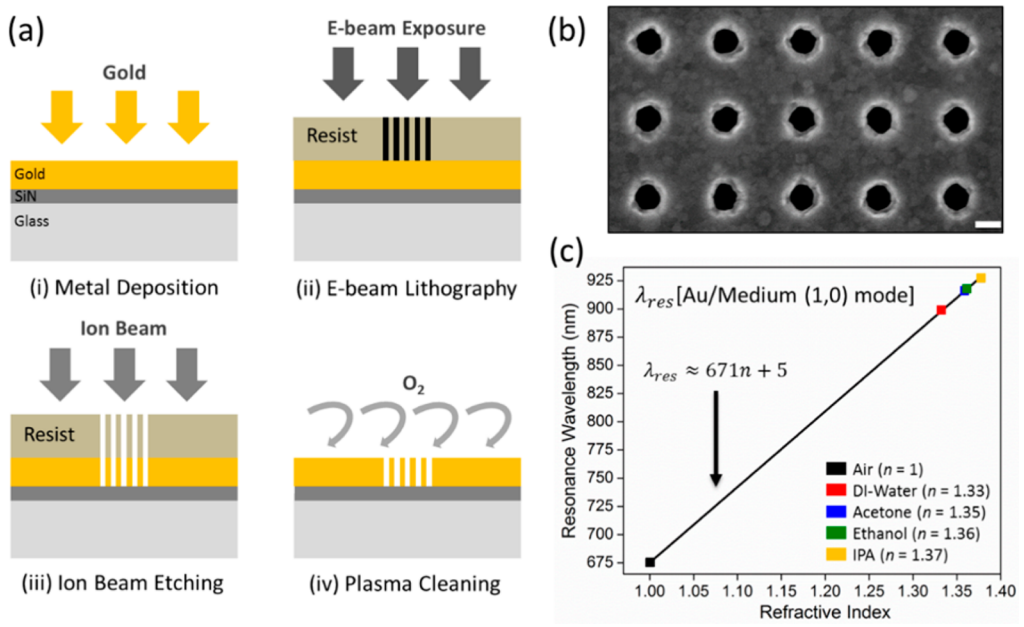

Figure 3. (a) Steps of the lift-off-free nanofabrication scheme. (b) SEM image of the fabricated nanoapertures on a hybrid substrate. Scale bar: 200 nm. (c) Resonance wavelength of Au/Medium(1,0) mode vs refractive indices of bulk solutions, $n_{\mathrm{DI-Water}} \approx 1.33$, $n_{\mathrm{Acetone}} \approx 1.35$, $n_{\mathrm{Ethanol}} \approx 1.36$, and $n_{\mathrm{IPA}} \approx 1.37$. Corresponding device parameters used in the experiments: hole diameter 200 nm, array periodicity 600 nm, thicknesses of the gold film and silicon nitride interlayer 120 and 90 nm, respectively.

Au/Glass modes. Electric field intensity profiles are calculated along the *xz*-cross section at $y = 0$, where the electric field intensity is maximum (see Figure S1 for the region where the cross-sectional electric field distributions are calculated). Magnetic field distributions (Figure 2c, left column) corresponding to Au/Medium(1,0) [Medium = Air] and Au/Glass(1,0) modes show the expected symmetric standing field pattern along the *x*-direction, which is due to two counter-propagating surface plasmons.[12] On the other hand, for the Au/Glass(1,1) mode, a diagonal standing wave pattern is observed due to the interference of multiple propagating surface plasmon excitations. For all the modes, hot spots along the *y*-direction are due to localized surface plasmon excitations. The magnetic field profiles clearly show that the transmission resonances uniquely incorporate both propagating and localized surface plasmons. On the basis of the electric field intensity distributions (Figure 2c, right column), plasmonic excitations for the Au/Medium(1,0) mode [Medium = Air] are confined at the top surface of the gold film and extend deep into air. In contrast, for Au/Glass(1,0) and Au/Glass(1,1) modes, near-fields are mostly concentrated at the gold/glass interface (Figure S1 shows these modes' dipolar characters through electric field intensity profiles calculated at the aperture plane).

Figure 2b shows that as the silicon nitride thickness increases, Au/Glass(1,0) and Au/Glass(1,1) modes (denoted with blue and red arrows, respectively) shift to longer wavelengths and their transmission intensities dramatically decrease. At thickness $t = 70$ nm, they are suppressed within the wavelength region of interest. The aperture system supports a single well-defined transmission resonance due to the excitation of the Au/Medium(1,0) mode [Medium = Air], as revealed by the magnetic field intensity distribution (Figure 2d, left column). The cross-sectional electric field profile (Figure 2d, right column) also demonstrates that the local electromagnetic fields are highly accessible, as they are mainly concentrated at the top surface of the gold film and extend into the medium in their vicinity. Here, a 70 nm silicon nitride interlayer is optically thin enough that it does not compromise the transmission intensity.[31]

FABRICATION OF NANOHOLE ARRAYS ON A HYBRID SUBSTRATE

In order to experimentally investigate the sensitivity of the nanohole arrays on a hybrid substrate, we utilize a lift-off-free fabrication scheme based on e-beam lithography. Figure 3a illustrates the fabrication steps. We first deposit 5 nm chromium and 120 nm gold (Leybold Optics LAB-600H e-beam evaporator) on a 500 μm thick fused silica coated with 90 nm low-pressure chemical vapor deposited silicon nitride film. We then perform E-beam lithography (Vistec EBPG5000) on a positive resist (495-A4 PMMA) to define nanohole arrays. After development, we etch the metal film with ion beam milling (Veeco Nexus IBE350) by using the resist as a mask. Finally, a plasma-cleaning step (TEPLA 300 plasma stripper) is performed to remove the remaining resist on the gold surface. Figure 3b shows the scanning electron microscopy (SEM) image of the fabricated nanoholes with 200 nm hole diameter and 600 nm array periodicity. We experimentally measure the sensitivity of the aperture system by monitoring the spectral variations within the Au/Medium(1,0) mode after introducing bulk solutions with different refractive indices, including deionized water $n_{\mathrm{DI-Water}} \approx 1.33$, acetone $n_{\mathrm{Acetone}} \approx 1.35$, ethanol $n_{\mathrm{Ethanol}} \approx 1.36$, and IPA (isopropyl alcohol) $n_{\mathrm{IPA}} \approx 1.37$ as shown in Figure 3c (see Figure S2 for details of the experimental setup utilized for the optical characterization of the nanohole arrays). In the optical characterization, the integration time is 200 ms with 10 averaged spectrum frames. The sensor measurements are performed over a 100 μm × 100 μm area.[32,33] With the measured resonance wavelength of the Au/Medium(1,0) mode for each bulk solution, a linear relationship is determined as follows: $\lambda_{\mathrm{res}} \approx 671\ n + 5$. This result shows that nanohole arrays on a hybrid substrate exhibit

DOI: 10.1021/acsphotonics.5b00242
ACS Photonics 2015, 2, 1167−1174

a refractive index sensitivity ($S = \Delta\lambda/\Delta n$) as large as 671 nm/RIU. Supporting spectrally sharp transmission resonances as narrow as ~16 nm, the aperture system shows a figure-of-merit value (FOM) ≈ 42. Note that this FOM value is calculated for bulk solutions, and it is more complex for biosensing applications, which depend on the size of the biomolecules and capturing mechanism.[34] These refractive index sensitivity and figure-of-merit values are highly advantageous for label-free biosensing applications demanding high sensitivities to change in surface conditions.

LABEL-FREE SENSING WITH NANOHOLES ON A HYBRID SUBSTRATE

In order to demonstrate the advantages of the nanohole system on a hybrid substrate over glass, we carry out label-free detection of protein bilayers by monitoring spectral variations within the plasmonic modes due to biomolecular bindings. In the experiments, we use a protein bilayer composed of protein A/G (from Pierce) and protein IgG (goat IgG from Sigma), which selectively bind on gold (see Supporting Information for protein chemistry and sample preparation techniques). Figure 4a and b show the spectral variations within the plasmonic modes supported by the nanohole arrays on glass and hybrid substrates, respectively. In Figure 4, green and red curves denote the transmission responses after the addition of protein A/G and protein IgG, respectively. Figure 4c shows the spectral shift amounts within each plasmonic mode (mean values with error bars calculated by adding twice the standard deviation from three independent experiments). Here, the Au/Medium-(1,0) mode [Medium = Air] of the hybrid substrate exhibits larger spectral shifts compared to the same mode supported by glass. Upon functionalization of nanoholes with a protein mono- and bilayer, containing 0.5 mg/mL protein A/G and 0.5 mg/mL protein IgG, for the hybrid substrate, the Au/Medium(1,0) mode [Medium = Air] shifts to longer wavelengths by ~4 nm and ~18 nm, whereas it shifts by ~3 and ~13 nm for glass. More importantly for the nanohole system on glass, the spectrum of Au/Medium(1,0) mode [Medium = Air] starts to overlap with the Au/Glass(1,1) mode. Furthermore, its transmission intensity decreases as it shifts to longer wavelengths. The larger sensitivity of the Au/Medium-(1,0) mode [Medium = Air] is due to its highly accessible large local electromagnetic fields resulting in a better spatial overlap between optical fields and biomolecules. In contrast, near-fields for Au/Glass modes are mostly inaccessible, as they are concentrated along the gold/glass interface. Consequently, with the coverage of protein A/G and protein IgG, the Au/Glass(1,1) [Au/Glass(1,0)] mode shifts only ~2 nm [~1 nm] and ~7 nm [~2 nm], respectively.

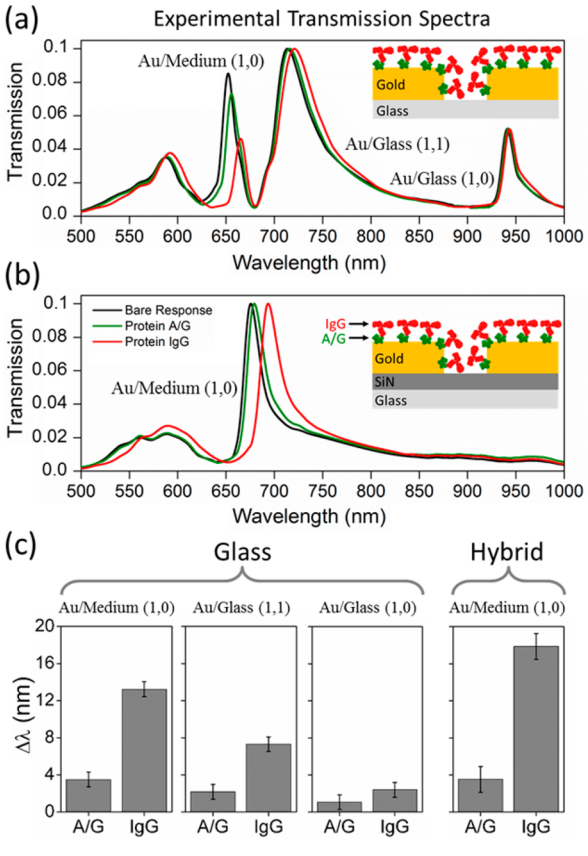

Figure 4. Experimental transmission spectra of the nanohole arrays on (a) glass and (b) hybrid substrates, where the gold surface is covered with a bilayer consisting of proteins A/G and IgG. (c) Spectral shift amounts for the plasmonic modes supported by the nanohole systems on glass and hybrid substrates.

SPECTRAL INTEGRATION METHOD FOR LOW LIMIT OF DETECTION

For label-free optical biosensors, one of the most common methods is to monitor the changes in the resonance wavelength. However, this approach is limited for determining minor refractive index changes, as it relies on spectral information only at a single wavelength. In contrast, using spectral data in a broad wavelength range near the resonance can significantly improve the sensitivity.[35,36] For example, Figure 5a and b show the experimental response of the nanohole system on the hybrid substrate embedded in 0.1% (red region) and 0.25% (black curve) ethanol solutions for the Au/Medium(1,0) mode [Medium = Ethanol] near its resonance within 8 and 2 nm wavelength ranges, respectively. For both cases, we do not observe a significant wavelength shift in the resonance wavelength with the resulting refractive index change of only 2×10^{-5} RIU. On the other hand as shown in Figure 5b, a collective red-shift along the left shoulder of the Au/Medium(1,0) [Medium = Ethanol] resonance is clearly observable. In order to utilize this shift, we integrate the transmission intensity of the Au/Medium(1,0) mode [Medium = Ethanol] within a spectral window for different refractive indices. In order to reliably differentiate the integral values corresponding to different refractive indices, we investigate the width and central wavelength of the spectral window used in the integration. Due to the asymmetric line-shape of the Au/Medium(1,0) mode [Medium = Ethanol] (arising from Fano-interferences as discussed in our earlier publication[10]), we observe that the spectral window covering the wavelengths between the resonance wavelength of the Au/Medium(1,0) mode [Medium = Ethanol] and the transmission minimum on the left-hand side (due to Wood's anomaly[10]) gives the most reliable integral variations (the spectral windows for both nanohole configurations are illustrated in Figure S3a and b). Figure 5c and d are the spectral integral values for the aperture systems on glass and hybrid substrates embedded in different refractive indices of bulk ethanol concentrations in DI-water ranging from 0.1% to 100%. As the refractive index of the medium increases with ethanol concentration, the spectrum red-shifts and the integral value gradually decreases. The two

DOI: 10.1021/acsphotonics.5b00242
ACS Photonics 2015, 2, 1167–1174

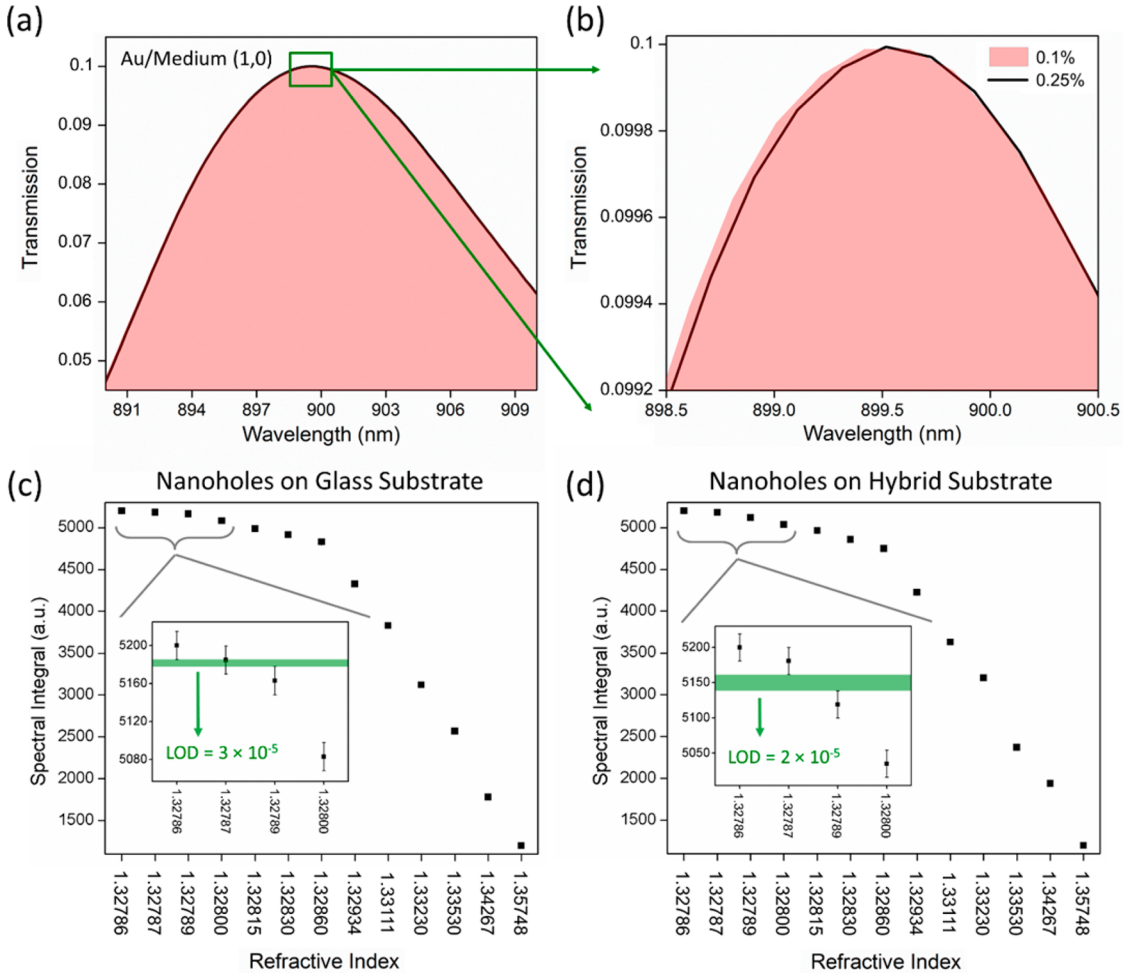

Figure 5. (a) Experimental transmission spectra of the nanohole arrays on a hybrid substrate embedded in 0.1% (red area) and 0.25% (black curve) ethanol concentrations shown for the Au/Medium(1,0) mode [Medium = Ethanol] within an 8 nm wavelength range at the resonance peak. (b) Transmission spectra zoomed within a 2 nm wavelength range denoted with a green square in part a to highlight the collective spectral shifts along the left-hand side of the Au/Medium(1,0) mode [Medium = Ethanol]. Spectral integral values calculated for the nanohole systems, embedded in different refractive indices of ethanol solutions, on (c) glass and (d) hybrid substrates, respectively. In the figures, zoomed-in images are used to show the limit-of-detection (LOD) of the aperture systems indicated with green.

figure insets show the zoom-in of the integral values corresponding to the lowest ethanol concentration. Here, the limit-of-detection (LOD) of the aperture system is defined as the minimum detectable refractive index change between the two distinguishable spectral integral values. We calculate the LOD (indicated by green) by adding twice the standard deviation to the mean integral value for the corresponding concentrations[37] obtained from three independent experiments. For the system on glass, a minimum detectable refractive index change of 3×10^{-5} RIU is obtained (integral values corresponding to 0.25% ethanol solution and DI-water, where n = 1.32789 and 1.32786, can be reliably differentiated). In contrast, the aperture system on the hybrid substrate supports 1.5-fold higher refractive index sensitivities with a detection limit as low as 2×10^{-5} RIU (integral values corresponding to 0.25% and 0.1% ethanol solutions, where n = 1.327 89 and 1.327 87, can be reliably differentiated). Recently, different methods to improve the refractive index sensitivity have been demonstrated utilizing plasmonics platforms combined with postprocessing methods, showing down to 10^{-6} RIU sensitivity levels.[33,38,39] In particular, the spectral integration method utilized here yields sensitivity values similar to the previously introduced centroid method.[40]

Using the spectral integration method, we successfully demonstrate label-free and real-time analysis of protein binding kinetics. Figure 6a and b show the photograph and the schematic illustration of the plasmonic biosensor integrated with dual-channel microfluidics used in the experiments (see also Figure S4 for the structure of the microfluidic chamber design). Initially, the sensors are functionalized with 0.5 mg/mL protein A/G. In channel I, we inject protein IgG (in a PBS solution). Channel II is used as a control, where we inject PBS (phosphate-buffered saline) with the same flow rate to determine the integral variations due to optical, mechanical, and chemical fluctuations. Figure 6c shows the time dependence of the integral value due to the binding of 1000 ng/mL protein IgG on protein A/G, reaching saturation after ~80 min. Next, the real-time behavior is fitted to an exponential equation to determine the association phase of protein IgG on protein A/G:[30]

$$I_t = I_0/(1 + e^{(k_a[IgG] - k_d)t}) \quad (2)$$

DOI: 10.1021/acsphotonics.5b00242
ACS Photonics 2015, 2, 1167–1174

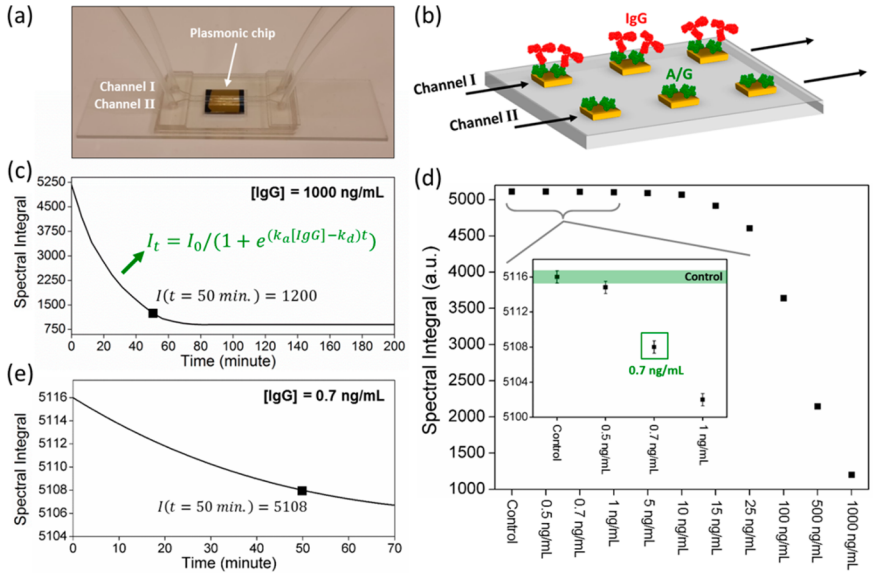

Figure 6. (a) Photograph and (b) schematic illustration of the plasmonic biosensor integrated with dual-channel microfluidics. Exponential behavior of the association phase of (c) 1000 ng/mL and (e) 0.7 ng/mL IgG on A/G determined by the spectral integral method. (d) Spectral integral value calculated for different IgG concentrations. The inset shows the limit-of-detection (LOD) of the aperture system denoted with green. Note that the initial integral values of the exponential curves are the same ($I(t = 0) = 5116$) for each IgG concentration such that we can reliably use the integral values at minute 50 for determining kinetics constants.

Here, k_a and k_d are the association and disassociation constants, respectively. The dissociation constant for mouse IgG on protein A/G is $k_d < 1 \times 10^{-6}$ s^{-1}, indicating that the composite is highly stable once it is formed, and a minimum amount of IgG will remain unbound.[41] Using the exponential fitting and k_d value for [IgG] = 1000 ng/mL, the association constant is calculated as $k_a = 2.37 \times 10^5$ M^{-1} s^{-1}. These results, comparable to conventional SPR, confirm that binding kinetics of proteins can be reliably extracted.[41] We next perform analysis at different IgG concentrations and determine the spectral integral values from the exponential curves at 50 min. Figure 6d shows the integral values for different IgG concentrations in the range between 0.5 to 1000 ng/mL. As shown in the zoom-in image in Figure 6d, inset, the integral value of the control determines the detection limit of our biosensing platform (indicated by green and calculated by adding twice the standard deviation to the mean integral value for the corresponding IgG concentrations). The results show that IgG concentrations can be reliably detected down to 0.7 ng/mL. This low limit-of-detection value is highly promising for label-free and real-time analysis of biomolecular binding kinetics at low analyte concentrations. Importantly as shown in Figure 6e, employing the spectral integration method, we measure biomolecular binding kinetics even at the 0.7 ng/mL level. For this IgG concentration, we calculate a similar association constant, $k_a = 2.29 \times 10^5$ M^{-1} s^{-1}.

CONCLUSION

In conclusion, we introduce a biosensing platform employing plasmonic nanohole arrays on a hybrid substrate. The system supports spectrally well-isolated and sharp optical responses, which are highly sensitive to surface conditions. Utilizing a high refractive index dielectric interlayer between gold film and glass, our nanoaperture system suppresses the additional plasmonic modes arising from the low refractive index of the transparent material utilized in the conventional nanohole designs. In the absence of spectral overlaps and amplitude variations, the strong optical response of the nanohole arrays on the hybrid substrate is easy to track for reliable monitoring of spectral variations. Furthermore, we improve the detection limit of our biosensing platform by integrating the spectral information in a large wavelength range instead of monitoring the changes only within the resonance wavelength and demonstrate a limit of detection as low as 2×10^{-5} RIU. We also successfully perform real-time detection of biomolecular binding kinetics at sub-1 ng/mL concentration, which is highly advantageous for label-free biosensing at ultralow analyte concentrations.

ASSOCIATED CONTENT

Supporting Information

The Supporting Information is available free of charge on the ACS Publications website at DOI: 10.1021/acsphotonics.5b00242.

Experimental details (PDF)

AUTHOR INFORMATION

Corresponding Author

*E-mail: hatice.altug@epfl.ch.

Notes

The authors declare no competing financial interest.

ACKNOWLEDGMENTS

We acknowledge Ecole Polytechnique Federale de Lausanne (EPFL) and Center of MicroNano Technology for financial support and nanofabrication. Y.E. acknowledges Brno University of Technology under the project CZ.1.07/2.3.00/30.0039.

REFERENCES

(1) Piliarik, M.; Sandoghdar, V. Direct optical sensing of single unlabelled proteins and super-resolution imaging of their binding sites. *Nat. Commun.* **2014**, *5*, 4495.

(2) Donath, E. Biosensors: Viruses for ultrasensitive assays. *Nat. Nanotechnol.* **2009**, *4*, 215−216.

DOI: 10.1021/acsphotonics.5b00242
ACS Photonics 2015, 2, 1167−1174

(3) Zhang, W.; Ganesh, N.; Block, I. D.; Cunningham, B. T. High sensitivity photonic crystal biosensor incorporating nanorod structures for enhanced surface area. *Sens. Actuators, B* **2008**, *131*, 279−284.
(4) Hendry, E.; Carpy, T.; Johnston, J.; Popland, M.; Mikhaylovskiy, R. V.; Lapthorn, A. J.; Kelly, S. M.; Barron, L. D.; Gadegaard, N.; Kadodwala, M. Ultrasensitive detection and characterization of biomolecules using superchiral fields. *Nat. Nanotechnol.* **2010**, *5*, 783−787.
(5) Gao, Y.; Gan, Q.; Bartoli, F. J. Spatially selective plasmonic sensing using metallic nanoslit arrays. *IEEE J. Sel. Top. Quantum Electron.* **2014**, *20*, 6900306.
(6) Qiu, L.; Zhang, T.; Jiang, J.; Wu, C.; Zhu, G.; You, M.; Chen, X.; Zhang, L.; Cui, C.; Yu, R.; Tan, W. Cell membrane-anchored biosensors for real-time monitoring of the cellular microenvironment. *J. Am. Chem. Soc.* **2014**, *136*, 13090−13093.
(7) Anker, J. N.; Hall, W. P.; Lyandres, O.; Shah, N. C.; Zhao, J.; Van Duyne, R. P. Biosensing with plasmonic nanosensors. *Nat. Mater.* **2008**, *7*, 442−453.
(8) Cetin, A. E.; Coskun, A. F.; Galarreta, B. C.; Huang, M.; Herman, D.; Ozcan, A.; Altug, H. Handheld high-throughput plasmonic biosensor using computational on-chip imaging. *Light: Sci. Appl.* **2014**, *3*, e122.
(9) Yanik, A. A.; Kamohara, O.; Artar, A.; Geisbert, T. W.; Connor, J. H.; Altug, H. An optofluidic nanoplasmonic biosensor for direct detection of live viruses from biological media. *Nano Lett.* **2010**, *10*, 4962−4969.
(10) Yanik, A. A.; Cetin, A. E.; Huang, M.; Artar, A.; Mousavi, S. H.; Khanikaev, A.; Connor, J. H.; Shvets, G.; Altug, H. Seeing protein monolayers with naked eye through plasmonic Fano resonances. *Proc. Natl. Acad. Sci. U. S. A.* **2011**, *108*, 11784−11789.
(11) Yanik, A. A.; Huang, M.; Artar, A.; Chang, T. Y.; Altug, H. Integrated nanoplasmonic-nanofluidic biosensors with targeted delivery of analytes. *Appl. Phys. Lett.* **2010**, *96*, 021101.
(12) Artar, A.; Yanik, A. A.; Altug, H. Fabry-Perot nanocavities in multilayered crystals for enhanced biosensing. *Appl. Phys. Lett.* **2009**, *95*, 051105.
(13) Eftekhari, F.; Gordon, R.; Ferreira, J.; Brolo, A. G.; Sinton, D. Polarization-dependent sensing of a self-assembled monolayer using biaxial nanohole arrays. *Appl. Phys. Lett.* **2008**, *92*, 253103.
(14) Huang, M.; Galarreta, B. C.; Cetin, A. E.; Altug, H. Actively transporting virus like analytes with optofluidics for rapid and ultrasensitive biodetection. *Lab Chip* **2013**, *13*, 4841−4847.
(15) Blanchard-Dionne, A. P.; Guyot, L.; Patskovsky, S.; Gordon, R.; Meunier, M. Intensity based surface plasmon resonance sensor using a nanohole rectangular array. *Opt. Express* **2011**, *19*, 15041−15046.
(16) Gao, H.; Henzie, J.; Odom, T. W. Direct evidence for surface plasmon-mediated enhanced light transmission through metallic nanohole arrays. *Nano Lett.* **2006**, *6*, 2104−2108.
(17) Schatz, G. C.; McMahon, J. M.; Gray, S. K. Tailoring the parameters of nanohole arrays in gold films for sensing applications. *Proc. SPIE* **2007**, *6641*, 664103.
(18) Thio, T.; Ghaemi, H. F.; Lezec, H. J.; Wolff, P. A.; Ebbesen, T. W. Surface-plasmon-enhanced transmission through hole arrays in Cr films. *J. Opt. Soc. Am. B* **1999**, *16*, 1743−1748.
(19) Dickson, W.; Wurtz, G. A.; Evans, P. R.; Pollard, R. J.; Zayats, A. V. Electronically controlled surface plasmon dispersion and optical transmission through metallic hole arrays using liquid crystal. *Nano Lett.* **2008**, *8*, 281−286.
(20) Cetin, A. E.; Altug, H. Fano resonant ring/disk plasmonic nanocavities on conducting substrates for advanced biosensing. *ACS Nano* **2012**, *6*, 9989−9995.
(21) Chang, T. Y.; Huang, M.; Yanik, A. A.; Tsai, H. Y.; Shi, P.; Aksu, S.; Yanik, M. F.; Altug, H. Large-scale plasmonic microarrays for label-free high-throughput screening. *Lab Chip* **2011**, *11*, 3596−3602.
(22) Liu, N.; Tang, M. L.; Hentschel, M.; Giessen, H.; Alivisatos, A. P. Nanoantenna-enhanced gas sensing in a single tailored nanofocus. *Nat. Mater.* **2011**, *10*, 631−636.
(23) Cinel, N. A.; Butun, S.; Ozbay, E. Electron beam lithography designed silver nano-disks used as label free nano-biosensors based on localized surface plasmon resonance. *Opt. Express* **2012**, *20*, 2587−2597.
(24) Paivanranta, B.; Merbold, H.; Giannini, R.; Buchi, L.; Gorelick, S.; David, C.; Loffler, J. F.; Feurer, T.; Ekinci, Y. High aspect ratio plasmonic nanostructures for sensing applications. *ACS Nano* **2011**, *5*, 6374−6382.
(25) Otte, A. A.; Estevez, M. C.; Carrascosa, L. G.; Gonzalez-Guerrero, A. B.; Lechuga, L. M.; Sepulveda, B. Improved biosensing capability with novel suspended nanodisks. *J. Phys. Chem. C* **2011**, *115*, 5344−5351.
(26) Acimovic, S. S.; Kreuzer, M. P.; Gonzalez, M. U.; Quidant, R. Plasmon near-field coupling in metal dimers as a step toward single-molecule sensing. *ACS Nano* **2009**, *3*, 1231−1237.
(27) Ruemmele, J. A.; Hall, W. P.; Ruvuna, L. K.; Van Duyne, R. P. A localized surface plasmon resonance imaging instrument for multiplexed biosensing. *Anal. Chem.* **2013**, *85*, 4560−4566.
(28) Acimovic, S. S.; Ortega, M. A.; Sanz, V.; Berthelot, J.; Garcia-Cordero, J. L.; Renger, J.; Maerkl, S. J.; Kreuzer, M. P.; Quidant, R. LSPR chip for parallel, rapid, and sensitive detection of cancer markers in serum. *Nano Lett.* **2014**, *14*, 2636−2641.
(29) Mazzotta, F.; Johnson, T. W.; Dahlin, A. B.; Shaver, J.; Oh, S. H.; Hook, F. Influence of the evanescent field decay length on the sensitivity of plasmonic nanodisks and nanoholes. *ACS Photonics* **2015**, *2*, 256−262.
(30) Coskun, A. F.; Cetin, A. E.; Galarreta, B. C.; Alvarez, D. A.; Altug, H.; Ozcan, A. Lensfree optofluidic plasmonic sensor for real-time and label-free monitoring of molecular binding events over a wide field-of-view. *Sci. Rep.* **2014**, *4*, 6789.
(31) Usoskin, A. I.; Popova, O. A. Silicon nitride films: Optical properties and possibility of applications in multilayer interference systems. *J. Appl. Spectrosc.* **1985**, *43*, 1268−1271.
(32) Zeng, B.; Gao, Y.; Bartoli, F. J. Rapid and highly sensitive detection using Fano resonances in ultrathin plasmonic nanogratings. *Appl. Phys. Lett.* **2014**, *105*, 161106.
(33) Im, H.; Sutherland, J. N.; Maynard, J. A.; Oh, S. H. Nanohole-based surface plasmon resonance instruments with improved spectral resolution quantify a broad range of antibody-ligand binding kinetics. *Anal. Chem.* **2012**, *84*, 1941−1947.
(34) Li, J.; Ye, J.; Chen, C.; Li, Y.; Verellen, N.; Moshchalkov, V. V.; Lagae, L.; Van Dorpe, P. Revisiting the surface sensitivity of nanoplasmonic biosensors. *ACS Photonics* **2015**, *2*, 425−431.
(35) Lee, K. L.; Wei, P. K. Enhancing surface plasmon detection using ultrasmall nanoslits and a multispectral integration method. *Small* **2010**, *6*, 1900−1907.
(36) Stewart, M. E.; Mack, N. H.; Malyarchuk, V.; Soares, J. A. N. T.; Lee, T. W.; Gray, S. K.; Nuzzo, R. G.; Rogers, J. A. Quantitative multispectral biosensing and 1D imaging using quasi-3D plasmonic crystals. *Proc. Natl. Acad. Sci. U. S. A.* **2006**, *103*, 17143−17148.
(37) Skoog, D. A.; Holler, F. J.; Crouch, S. R. *Principles of Instrumental Analysis*; Thomson Higher Education: Belmont, CA, 2007.
(38) Zeng, B.; Gao, Y.; Bartoli, F. J. Differentiating surface and bulk interactions in nanoplasmonic interferometric sensor arrays. *Nanoscale* **2015**, *7*, 166−170.
(39) Gao, Y.; Xin, Z.; Zeng, B.; Gan, Q.; Cheng, X.; Bartoli, F. J. Plasmonic interferometric sensor arrays for high performance label-free biomolecular detection. *Lab Chip* **2013**, *13*, 4755−4764.
(40) Dahlin, A. B.; Tegenfeldt, J. O.; Hook, F. Improving the instrumental resolution of sensors based on localized surface plasmon resonance. *Anal. Chem.* **2006**, *78*, 4416−4423.
(41) Bronner, V.; Tabul, M.; Bravman, T. Rapid screening and selection of optimal antibody capturing agents using the ProteOn XPR36 protein interaction array system. *Bio-Rad Technical Note*, **2006**, *5820*.

DOI: 10.1021/acsphotonics.5b00242
ACS Photonics 2015, 2, 1167−1174